buildings

MDPI

Article

DEM-Based Simulation Study on the Operational Performance of a Single Horizontal Shaft Forced-Action Mixer

Haipeng Yang [1], Guanguo Ma [2,*] and Wei Zhao [1]

[1] Zaozhuang Mining Group Xin'an Coal Industry Co., Ltd., Zaozhuang 277800, China
[2] College of Safety and Environmental Engineering, Shandong University of Science and Technology, Qingdao 266590, China
* Correspondence: ma156154682@126.com

Abstract

This study conducts a numerical simulation of the working performance of a single horizontal shaft forced mixer using the Discrete Element Method (DEM). It systematically investigates the effects of blade installation angle, feeding method, mixing speed, and coarse aggregate particle size on the mixing uniformity. A 1:2 scale model was developed, incorporating Newton's laws of motion and a soft-sphere contact model to simulate the particle trajectories and interactions during mixing. The results indicate that top–bottom feeding enhances mixing efficiency significantly by forming vertical convective circulation, achieving a mixing uniformity above 0.9. A moderate rotation speed of 30 rpm provides the best balance between energy consumption and mixing performance. As the coarse aggregate size increases (from 9 mm to 15 mm), the enhanced particle inertia leads to a decrease in mixing uniformity (from 0.9 to 0.6). Additionally, the discrepancy between simulation and experimental results is less than 0.1, validating the reliability of the model. This research offers theoretical guidance for the structural optimization and parameter selection of single-shaft mixers, contributing to improved mixing efficiency and concrete quality in engineering applications.

Keywords: discrete element method; single-shaft mixer; mixing uniformity; mixing parameter optimization; numerical simulation

Academic Editor: Giuseppina Uva

Received: 12 June 2025
Revised: 21 July 2025
Accepted: 23 July 2025
Published: 24 July 2025

Citation: Yang, H.; Ma, G.; Zhao, W. DEM-Based Simulation Study on the Operational Performance of a Single Horizontal Shaft Forced-Action Mixer. *Buildings* **2025**, *15*, 2627. https://doi.org/10.3390/buildings15152627

1. Introduction

The rapid development of infrastructure projects such as underground coal mining, building construction, tunnel engineering, and roadworks has significantly driven the research and improvement of concrete mixing equipment. According to the number of mixing shafts, forced mixers can be categorized into three main types: single horizontal shaft, double horizontal shaft, and vertical shaft mixers. Among them, the single horizontal shaft concrete mixer is widely used due to its compact structure, ease of operation, and suitability for small- to medium-scale engineering applications [1,2]. Evolving from early drum mixers, forced mixers aim to achieve more uniform concrete mixing through mechanical agitation.

With the increasing demand for higher concrete quality and construction efficiency, the technology of single-shaft mixers has seen continuous advancement [3–5]. Numerous scholars have conducted studies on different types of mixers. In the field of horizontal shaft mixers, foreign research began relatively early, especially focusing on asphalt mixture mixing and sampling accuracy. Experimental results have shown that in horizontal shaft

mixers, mixtures exhibit irregular motion between the two shafts and horizontal cyclic motion along the mixer wall. The magnitude of this circulation is influenced by the angle between the blade surface and the motion direction [6,7]. At Chang'an University, Feng and his team [8,9] conducted extensive theoretical analyses and model tests on the motion characteristics of mixtures in horizontal shaft mixers. They focused on how structural and operational parameters affect mixing quality, identifying optimal value ranges and combinations of those parameters. Liu [10] developed a mathematical model for asphalt mixture mixing in horizontal mixers, analyzing the key factors influencing mixture uniformity. Experimental verification revealed that structural, operational, and usage parameters are the most critical factors. Wang [11] analyzed the structure and operating principle of single horizontal shaft Total Mixed Ration (TMR) mixers, identifying blade angle and rotational speed as key parameters for improving mixing efficiency, and determined their optimal combination through experiments. Laurent et al. [12] applied Positron Emission Particle Tracking (PEPT) to study particle motion in single-blade mixers, revealing a correlation between shaft torque and particle flow patterns. Their findings showed that mixing effectiveness is highly dependent on the fill level and blade motion pattern. Li [13] investigated the collapse flow of granular columns in fluids, analyzing the partition characteristics and evolution of different flow behaviors and establishing scaling laws for flow distance and duration.

Cundall and his team [14,15] proposed the Discrete Element Method (DEM), enabling accurate tracking of individual particle trajectories and forces in granular flows and detailed recording of inter-particle and particle–boundary contact and collisions. DEM is particularly applicable for studying particle behavior during mixing, offering a powerful tool to deepen the understanding of mixing mechanisms. Cai et al. [16] used DEM to verify the mixing behavior of monodisperse particles, providing data support for large-scale industrial applications. Lischka et al. [17] used DEM to analyze the dispersion of particle agglomerates in a vertical stirred tank, finding that increasing rotation speed improves mixing uniformity, though the effect plateaus beyond a certain speed. In the field of dry powder mixing, the Discrete Element Method (DEM) has become a critical tool for optimizing industrial mixer designs, as demonstrated by simulation studies on dry mixing processes for lithium-ion battery cathode materials [17] and parameter optimization of plow mixers [18]. For cohesive particle systems, DEM simulations reveal the significance of the Bond number similarity principle in predicting mixing behavior [19], while differences in particle flowability decisively influence residence time and mixing homogeneity in twin screw mixers [20]. Balancing power consumption and mixing efficiency remains a key challenge in mixer design; studies show that adjusting rotational speed and speed ratio in planetary mixers enhances mixing performance but significantly increases energy consumption [21], whereas soil mixer optimization requires simultaneous consideration of the Lacey mixing index and power consumption [22]. For non-spherical particles, coordinated optimization of paddle angle (30–45°) and rotational speed in paddle mixers can strengthen diffusion-dominated mixing mechanisms [23]; meanwhile, near-nozzle continuous mixers for 3D concrete printing necessitate the spatial Lacey mixing index (SLMI) to evaluate local mixing uniformity [24].

Despite significant progress in DEM-based mixer optimization, current research predominantly focuses on large-scale industrial or multi-shaft mixers, with insufficient attention to compact single-shaft systems essential for small-to-medium projects. Existing DEM approaches also suffer accuracy limitations when simulating complex scenarios involving diverse materials and dynamic parameters. To bridge these gaps, this study pioneers a focused investigation on small-scale single horizontal shaft forced mixers ($\leq$0.4 m drum diameter), establishing three objectives: (1) developing a validated DEM framework tai-

lored for granular dynamics in these systems; (2) quantifying the impact of understudied parameters—blade angle, radial position, feeding method, coarse aggregate size, and rotational speed—on mixing uniformity; and (3) identifying optimal operational configurations for enhanced concrete production efficiency. The novelty lies in the following: a pioneering focus on compact single-shaft mixers contrasting prior large-system studies; rigorous experimental validation (error <0.1) of multi-parameter interactions; and an innovative scaled DEM framework (1:2 geometrically with particle size consistency) enabling computationally efficient yet industrially representative simulations. This work delivers actionable insights for structural refinement and energy-efficient operation of single-shaft mixers in construction applications.

2. DEM Simulation Model

2.1. Particle Motion Model

In this study, uniformly sized spherical particles were investigated, and the translational and rotational motions of individual particles were tracked based on Newton's second law of motion. The particle dynamics are governed by the conservation of linear and angular momentum, expressed for particle i by the following equations:

$$m_i \frac{dv_i}{dt} = \sum_{j=1,i\neq j}^{N} f_{cij} + m_i g \tag{1}$$

$$I_p \frac{d\omega_i}{dt} = \sum_{j=1,i\neq j}^{N} T_{pij} \tag{2}$$

Here, m_i and v_i represent the mass and velocity of particle i, respectively, and $\mathbf{f}_c$ denotes the contact force. $\mathbf{T}_p$ is the torque generated by the tangential component of the contact force. I_p and $\boldsymbol{\omega}_i$ are the moment of inertia and angular velocity of the particle, respectively. The forces and torques between particles are summed over the N particles in contact with particle i. The inter-particle contact forces are calculated using the soft-sphere model.

2.2. Contact Model of Particles

The Hertz–Mindlin contact model with damping was selected for its proven accuracy in simulating granular flows involving both elastic and dissipative collisions [25,26]. This model effectively captures two critical aspects of concrete mixing dynamics: (1) the nonlinear elastic recovery during particle collisions governed by Hertzian theory ($\delta^{3/2}$ dependence), and (2) the inelastic energy dissipation during sustained contacts, which dominates the rheological behavior of cohesive granular materials. During the collision of two particles, the contact force $\mathbf{f}_c$ is decomposed into normal ($\mathbf{f}_{cn,ij}$) and tangential ($\mathbf{f}_{ct,ij}$) components, as illustrated in Figure 1. The elastic part of the normal contact force $\mathbf{f}_{cn}$ is modeled using a nonlinear spring, where the force is proportional to the contact stiffness k_n and the normal overlap $\delta_n^{3/2}$. These forces are expressed as given in the following:

$$f_{cn,ij} = \left(-k_n \delta_{nij}^{3/2} - \eta_n v_{rij} n_{ij}\right) n_{ij} \tag{3}$$

$$f_{ct,ij} = -k_t \delta_{tij}^{3/2} - \eta_t v_{tij} \tag{4}$$

Here, i,j = particle indices; n,t = normal/tangential components; r = relative motion. k_n, k_t, and η_n, η_t denote the normal/tangential spring stiffness and damping coefficients, respectively. δ_{nij} and δ_{tij} represent the normal and tangential overlap displacements between particles i and j. $\mathbf{n}_{ij}$ is the unit vector connecting particle centers (direction $i \rightarrow j$). The second terms in Equations (3) and (4) ($-\eta_n v_{rij} \mathbf{n}_{ij}$ and $-\eta_t v_{tij}$) represent viscous dissipation:

These dissipation terms critically govern energy decay during collisions: higher η values increase damping, reducing particle rebound and promoting sustained contacts

essential for homogeneous mixing. For concrete simulations, appropriate η calibration ensures realistic aggregation behavior without artificial particle clustering.

The contact parameters used in this study are listed in Table 1.

Table 1. Contact parameters for DEM simulations.

Parameter	Value	Unit
Normal stiffness	1.2×10^6	$N/m^3/2$
Tangential stiffness	0.4×10^6	$N/m^3/2$
Normal damping coeff.	8.5×10^3	N·s/m
Tangential damping coeff.	2.4×10^3	N·s/m
Particle density	2500	kg/m^3

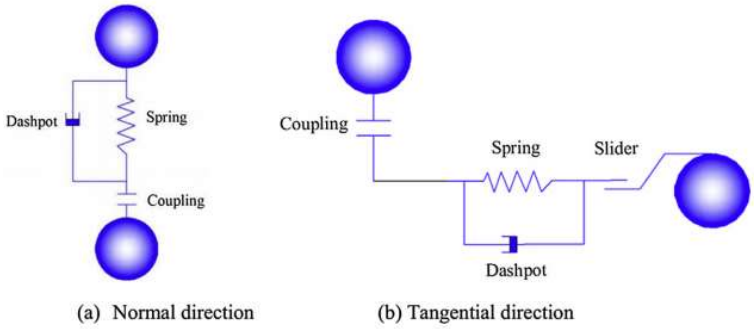

Figure 1. Contact force between two ideal dipoles predicted with a soft sphere model.

All DEM simulations were performed using EDEM 2022.2 (DEM Solutions Ltd., Edinburgh, UK) [27], a commercial software package implementing the soft-sphere contact model described in Equations (1)–(4). The solver utilized a variable time step (10^{-5}–10^{-4} s) based on Rayleigh wave propagation criteria to ensure numerical stability. Particle generation and motion analysis followed EDEM's standard material handling module with GPU acceleration.

3. Physical Model Construction and Simulation Parameters

3.1. Mixer Model

In this study, a prototype of a single-shaft forced concrete mixer was independently designed and constructed at a 1:2 scale, as shown in Figure 2, with the structural design diagram illustrated in Figure 3. The core components of the prototype include a drive motor, transmission system, mixing blades, and mixing drum. The prototype components were constructed using the following materials: the mixing drum was made of transparent poly(methyl methacrylate) (PMMA, thickness: 10 mm) for visual observation; blades and shaft were fabricated from stainless steel (AISI 304, Belonging to universal materials, supplied by multiple manufacturers); and the support frame used structural steel (ASTM A36, Belonging to universal materials, supplied by multiple manufacturers). The drive system consisted of a 1.5 kW three-phase AC motor (model: YE2-100L-4, Shanghai Dedong Electric Machinery Factory, Shanghai, China) with a gear reducer (ratio 1:48) to achieve operational speeds of 20–40 rpm, controlled by a variable-frequency drive (INVT GD200-0015G/2R2P-4, Shenzhen Yingweiteng Electric Co., Ltd., Shenzhen, China). To ensure the prototype achieved the desired mixing performance, the design process strictly referred to structural parameters from practical engineering mixing equipment. The layout, spacing, and angles of the mixing blades were carefully optimized. The mixing drum was made from transparent materials, allowing clear observation of the concrete's mixing state and flow behavior during experiments.

Figure 2. Test prototype.

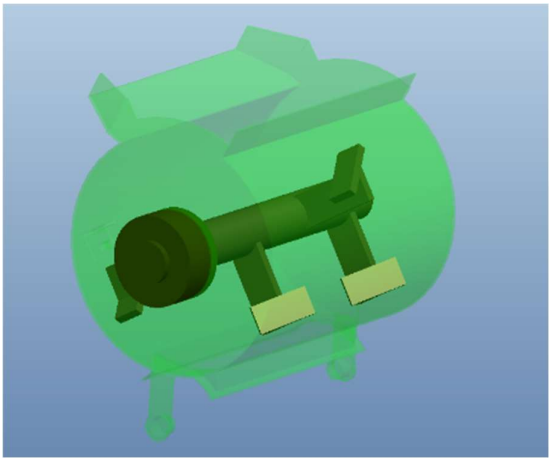

Figure 3. Structural design of the mixer prototype.

To balance computational cost with simulation accuracy, a scaled model was adopted in this study for the numerical modeling of the single-shaft mixer. This model was downscaled to a 1:2 ratio based on the actual mixer dimensions, ensuring accurate geometric representation while enabling completion of simulation tasks within a reasonable computational time. Scaled models are commonly used in particle material simulations, especially in complex multi-particle systems, where scaling can significantly reduce the number of simulated particles and computational complexity, thereby lowering computational costs. Although differences exist between scaled and full-scale physical models, proper scaling and experimental validation can ensure that simulation results maintain good representativeness and practical relevance. Table 2 compares the main geometric dimensions of the full-scale mixer and the scaled model. Through simplification and scaling of the mixer geometry, the model retains the key structural features of the mixing drum and blades, including blade quantity, angles, and positioning, while ensuring that the particle motion trajectories during mixing remain consistent with actual operating conditions.

Table 2. Comparison of dimensions between actual mixer and scaled model.

Parameter	Full-Scale Dimensions (mm)	Scaled Model Dimensions (mm)
Mixing drum diameter	800	400
Mixing drum height	880	440
Blade length	300	150
Blade width	100	50
Distance from blade to shaft	220	110
Blade installation angle	45°	45°

3.2. Evaluation Index (Mixing Uniformity)

Mixing uniformity is a critical metric for assessing the homogeneity of materials and serves as a key parameter for evaluating concrete performance. To intuitively quantify the degree of particle mixing, various evaluation methods are commonly used, including standard deviation, coefficient of variation, coordination number, Lacey index, and statistical entropy. Each method has its own applicable scope: The coefficient of variation is mainly suited for axial mixing and industrial mixing processes where material sampling is convenient. The coordination number is typically used in heat transfer models between interacting particles and requires high particle count statistics. The Lacey index is primarily applied to radial mixing. This method, proposed by Lacey in 1954 based on statistical theory, provides a quantitative measure of mixing degree. Based on the standard deviation approach and the actual mixing behavior, the Lacey index can be calculated using the following equation:

$$\mathrm{M} = \frac{S_0^2 - S^2}{S_0^2 - S_r^2} \tag{5}$$

In the equation, S^2 is the variance of the actual mixture of the two materials; S_0^2 is the variance when the two materials are completely segregated; and S_r^2 is the variance when the two materials are completely randomly mixed.

4. Results Analysis and Discussion

4.1. Numerical Simulation of Mixer Operating Characteristics

Figure 4 illustrates the velocity distribution of material particles during the mixing process under the conditions of a rotation speed of 30 rpm, maximum coarse aggregate size of 9 mm, and top–bottom filling. As shown in the figure, at the initial stage of mixing, the particle velocity is primarily concentrated near the mixing blades, forming high-velocity zones. This indicates that particles are rapidly displaced or lifted by the blades. However, mixing at this stage is still insufficient, as particle movement is largely localized around the blades, reflecting partial mixing behavior in the early phase. As mixing time progresses to 30 s and 40 s, the velocity distribution of particles becomes more widespread. An increase in the green and yellow regions indicates that more particles are mobilized and participate in the overall mixing within the container. At this point, particle overturning and mixing across different spatial regions are intensified, significantly enhancing mixing efficiency. This evolution in velocity distribution not only reflects the dynamic behavior of particles during mixing but also highlights the strong driving effect of the blades on particle motion in the initial stage. With further mixing up to 50 s and 60 s, the particle velocity distribution tends to become more uniform. The regions of high velocity shrink significantly, while the areas occupied by particles with lower velocities expand.

This change indicates that as mixing time increases, the mixer's influence on particle blending gradually shifts from localized mixing to overall homogenization, ultimately reaching an optimal mixing state. Additionally, at 60 s, the particle velocity distribution stabilizes, suggesting that the mixing process is nearing completion and the particles are well mixed. The uniformity of velocity distribution at this stage confirms the critical role of mixing time in determining mixing efficiency, demonstrating that under a rotational speed of 30 rpm, a mixing duration of 60 s is sufficient to achieve a well-mixed material state. Overall, the variation in particle velocity during mixing is not only a function of time but is also influenced by the mixer's structural design, rotational speed, and material properties.

Figure 5 illustrates the mixing behavior of material particles during the process under conditions of 30 rpm rotation speed, 9 mm maximum coarse aggregate size, and top–bottom filling. At the initial stage, fine aggregates are primarily concentrated at the bottom of

the mixer, while coarse aggregates rest above them, with minimal contact and mixing between the two. At this stage, the movement of the mixing blades primarily affects the fine aggregates, causing them to flow and begin interacting with the coarse aggregates due to pushing and shearing actions. However, due to the short mixing time, the materials remain in a distinctly stratified structure, and the initial mixing of coarse aggregates is relatively poor.

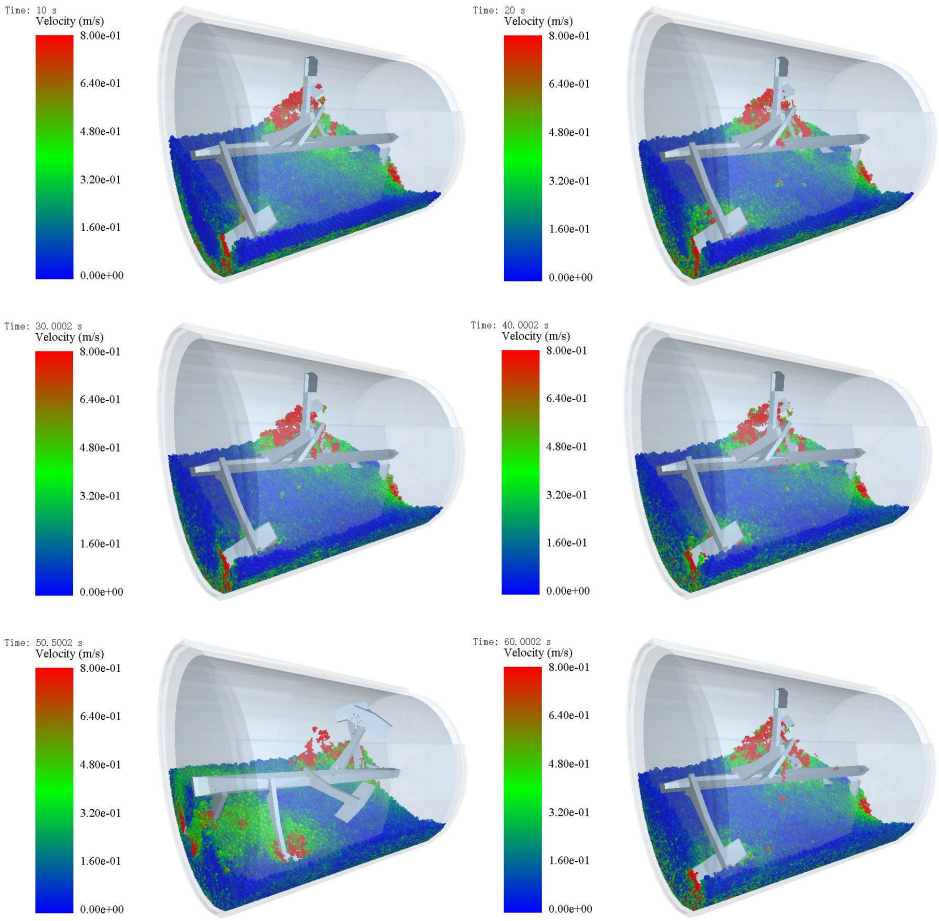

Figure 4. Velocity distribution of material particles during mixing.

By 10 s into mixing, a significant improvement in the mixing state is observed. The fine aggregates, propelled upward by the mixing blades, begin to make strong contact and mix with the coarse aggregates. During this process, the interface between the two aggregate types becomes increasingly indistinct, indicating effective mixing action. Meanwhile, the rotation and overturning of the blades induce noticeable flow and mixing trends within the container. As the mixing time extends further, the distribution of materials across different zones becomes more uniform. At 60 s, the mixing between fine and coarse aggregates improves substantially, presenting a more homogeneous spatial distribution. The originally distinct layered structure has been disrupted, and the materials form a uniformly distributed mixture throughout the mixer. The shearing and overturning action of the blades ensures that both fine and coarse aggregates are thoroughly blended across all positions, reaching an ideal mixing state.

This observed mixing behavior demonstrates that under the current mixing conditions, a 60 s duration effectively achieves a uniform material blend. In summary, Figure 5 presents the dynamic mixing process over different time intervals, showing how the initially layered fine and coarse aggregates are progressively transformed into a homogeneous mixture under the influence of the mixing blades. The increase in mixing time contributes

significantly to the improvement of both uniformity and stability. This simulation analysis provides valuable insights for optimizing mixer design and enhancing mixing efficiency and quality in practical engineering applications.

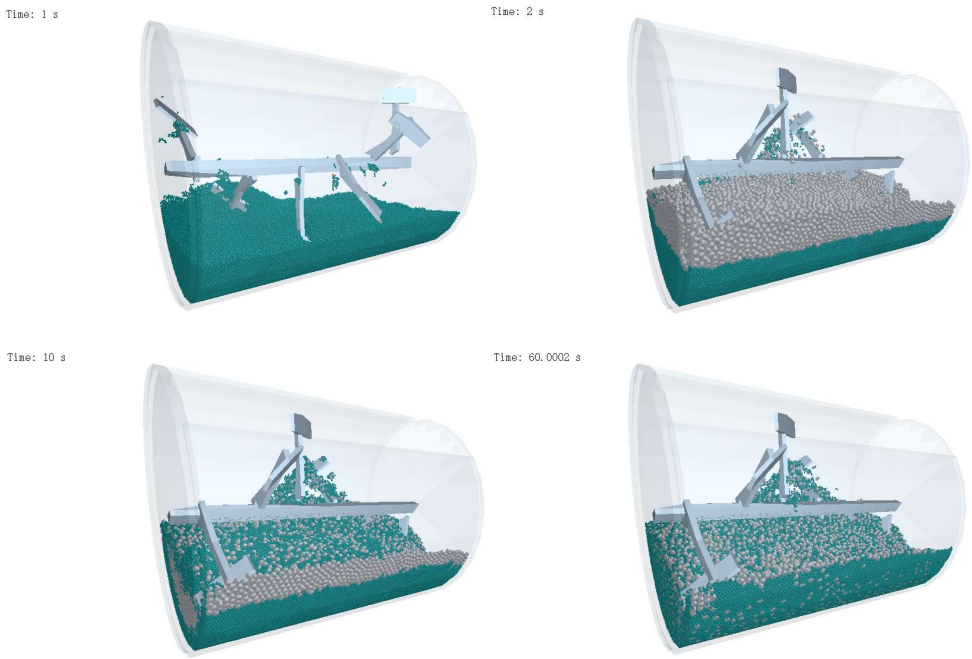

Figure 5. Mixing state of materials in the mixer at different times.

Mixing uniformity metrics (Section 3.2) were quantified using EDEM's Analyst module with grid-based sampling (cell size = 2 × mean particle diameter). Particle trajectory animations were rendered via EDEM's Creator visualization toolkit. Figure 6 illustrates the influence of three key factors—filling method, rotational speed, and coarse aggregate particle size—on mixing uniformity. As a critical indicator of mixing performance, analyzing the variation of mixing uniformity under these conditions helps to better understand the specific effects of each factor. The following discussion provides a detailed analysis of how each factor affects mixing uniformity.

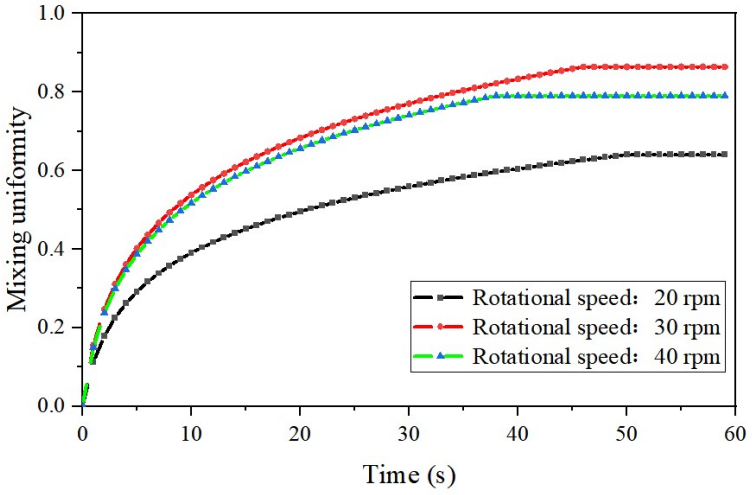

Figure 6. The trend of mixing degree over time at different rotational speeds.

Figure 6 demonstrates the dynamic influence of rotational speed (20 rpm, 30 rpm, or 40 rpm) on mixing homogeneity. During the initial phase (0–20 s), the mixing degree

increased rapidly under all rotational speeds, with 30 rpm exhibiting significantly faster growth than the other two conditions. At 20 rpm, the insufficient shear force resulted in weak particle convection, achieving only a 0.6 mixing degree at 60 s. Although 40 rpm reached its peak value (0.85) at 30 s, a slight decline occurred subsequently due to secondary segregation induced by centrifugal force. The 30 rpm condition demonstrated optimal dynamic balance: its blade shear force sufficiently drove vertical convection cycles while avoiding excessive turbulence, maintaining a stable mixing degree above 0.9 after 50 s. These curves validate the core mechanism of "moderate rotational speed"—excessively low speed (20 rpm) limits particle diffusion, while excessively high speed (40 rpm) intensifies collision energy consumption and segregation risks.

On the left side of Figure 7, the blue line graph shows the effects of three different filling methods—front–back, top–bottom, and left–right—on mixing uniformity. It can be observed that both the front–back and top–bottom filling methods yield relatively high mixing uniformity values, both approaching or exceeding 0.8. In contrast, the left–right filling method results in a significantly lower mixing uniformity of around 0.4. This demonstrates that the filling method has a pronounced impact on the effectiveness of the mixing process. Specifically, the front–back and top–bottom filling methods align better with the motion direction of the mixing blades, promoting stronger convective circulation during the mixing process. This circulation facilitates more uniform particle distribution within the mixer, reduces localized accumulation, and minimizes material stratification, thereby enhancing overall mixing uniformity. On the other hand, the left–right filling method creates an initial material distribution that is misaligned with the blade motion, which hinders the formation of effective convection early in the mixing process, ultimately leading to poor mixing uniformity. These results indicate that in practical applications, priority should be given to front–back or top–bottom filling methods to improve both mixing efficiency and uniformity.

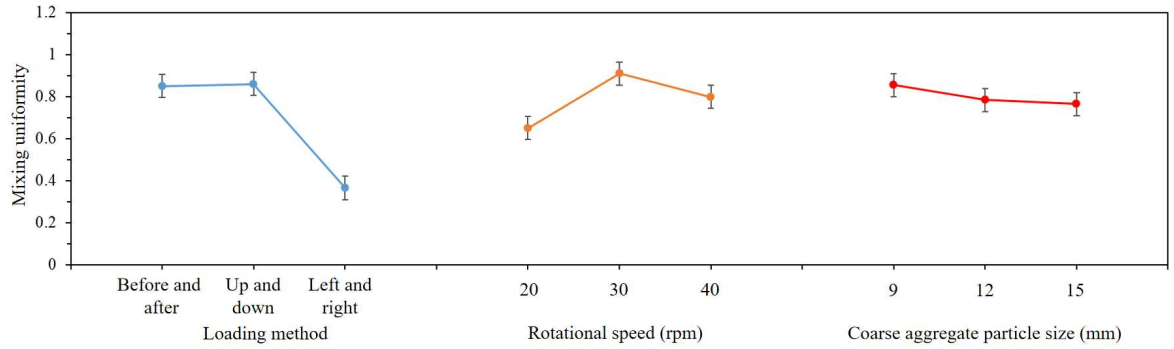

Figure 7. Effect of different factors on material mixing degree.

The center section of Figure 7, represented by the orange line graph, shows the effect of different rotational speeds (20 rpm, 30 rpm, and 40 rpm) on mixing uniformity. As rotational speed increases, the mixing uniformity improves accordingly. At 20 rpm, the mixing uniformity is the lowest, around 0.6. When the speed increases to 30 rpm, the mixing uniformity improves significantly, reaching close to 0.9. However, at 40 rpm, the mixing uniformity slightly decreases to about 0.85, though still remaining at a relatively high level. This suggests that moderate-speed mixing (30 rpm) most effectively enhances uniformity. At lower speeds, the shearing and pushing actions of the blades are relatively weak, making it difficult to adequately agitate and distribute the materials. At higher speeds, although mixing efficiency improves, the increased turbulence and particle collisions may lead to uneven particle distribution, adversely affecting the mixing uniformity. Therefore, in practical mixing operations, it is essential to select an appropriate rotational speed based

on the material properties and mixing requirements to achieve a balance between mixing efficiency and uniformity. Under the experimental conditions in this study, the moderate speed of 30 rpm demonstrates optimal performance.

On the right side of Figure 6, the red line graph shows the impact of different coarse aggregate sizes (9 mm, 12 mm, and 15 mm) on mixing uniformity. A clear trend is observed: as the particle size increases, the mixing uniformity decreases. With a 9 mm particle size, the highest uniformity is achieved, close to 0.9. For 12 mm and 15 mm aggregates, the uniformity decreases progressively to 0.75 and 0.6, respectively. This trend indicates that larger coarse aggregates possess greater mass and inertia, making them more difficult to mobilize effectively with the mixing blades, which limits inter-particle mixing. Moreover, larger particles are more likely to accumulate locally during mixing, further reducing uniformity. Therefore, selecting an appropriate coarse aggregate size is essential in practical engineering to ensure sufficient mixing and improve uniformity. Under the conditions of this experiment, the 9 mm aggregate size yields the best performance, indicating that smaller particle sizes are more conducive to achieving uniform mixing.

Figure 8 presents a comparison between experimentally measured and numerically simulated mixing uniformity under varying conditions of filling method, rotational speed, and coarse aggregate particle size. For different filling methods, both experimental and simulated mixing uniformity under the front–back filling condition are close to 0.8, with the experimental value slightly lower than the simulated one. The error is minimal, approaching zero, indicating a high level of agreement between the simulation and experimental results. Under the top–bottom filling condition, both values increase slightly compared to the front–back case, though the experimental value remains slightly higher than the simulated one. In contrast, under the left–right filling condition, the mixing uniformity drops significantly, with both the experimental and simulated values falling below 0.4. For varying rotational speeds, both experimental and simulated mixing uniformity are low at 20 rpm, with the experimental value slightly exceeding the simulated result. At 30 rpm, both values increase markedly, reaching nearly 0.9, and the deviation between them is minimal. At 40 rpm, mixing uniformity slightly decreases but remains at a high level, and the error between the experimental and simulated values is close to zero. Regarding coarse aggregate particle size, at 9 mm, both experimental and simulated mixing uniformity are high, close to 0.9. At 12 mm, the uniformity declines slightly, but the experimental value remains higher than the simulated one, with a small deviation. At 15 mm, the mixing uniformity further decreases, with the experimental value slightly lower than the simulated result. In all cases, the errors between experimental and simulated results are less than 0.1, which falls within an acceptable range. This confirms that the simulation results exhibit a high degree of consistency with the experimental data, validating the accuracy and reliability of the DEM-based numerical model used in this study.

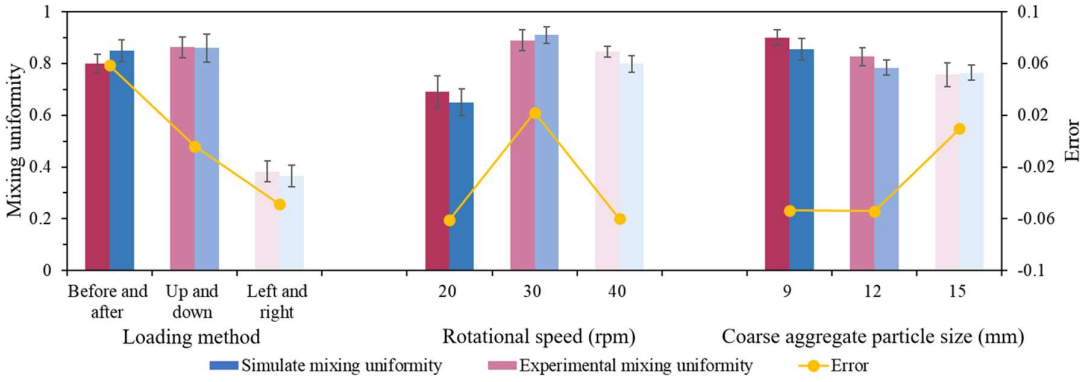

Figure 8. Comparative analysis of simulated mixing degree and experimental mixing degree.

4.2. Effect of Different Operating Modes on Mixer Performance

4.2.1. Effect of Different Filling Methods on Mixing Performance

In the numerical simulation study of concrete mixers, different material filling methods have a significant impact on the mixing performance. Figure 9 compares the mixing results under three filling strategies: front–back, top–bottom, and left–right, showing distinct differences in material distribution at 2 s and 60 s. Comparative analysis reveals that the front–back and top–bottom filling methods clearly outperform the left–right method, with the differences primarily observed in the initial material distribution and the effectiveness of blade action during the early mixing phase. Specifically, in the front–back filling method, materials are initially concentrated in the front and rear regions of the mixer (at 2 s). The rotation and overturning of the blades rapidly mobilize the material, forming a strong front-to-back convective circulation. The shearing and pushing actions of the blades effectively accelerate material redistribution, leading to a more homogeneous state by 60 s. This method fully utilizes the directional motion of the blades, resulting in relatively better mixing outcomes.

(**a**) Front–back filling

(**b**) Top–bottom filling

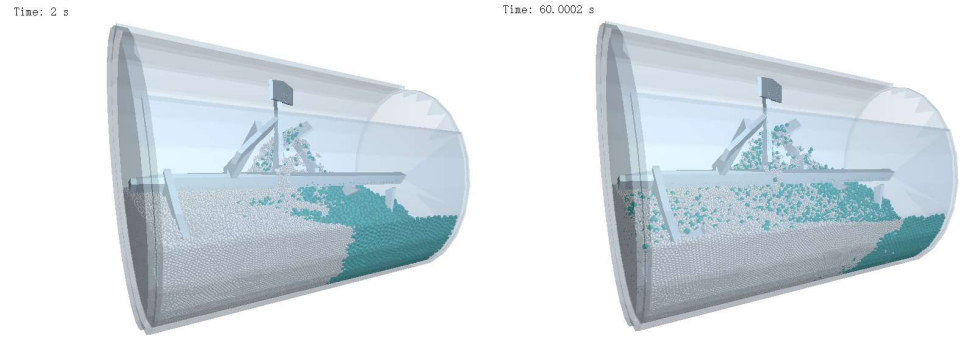

(**c**) Left–right filling

Figure 9. Final mixing effect under different material filling methods.

Similarly, in the top–bottom filling method, materials are initially distributed in the upper and lower sections of the mixing container. The rotation of the blades quickly establishes vertical convective flow, drawing materials into the mixing zone in a short time.

This strong vertical circulation not only enhances the mixing rate but also promotes uniform distribution of different particle types along the vertical axis. By 60 s, the mixing uniformity achieved by the top–bottom method is comparable to that of the front–back method, demonstrating its ability to fully leverage the blades' vertical shearing and overturning effects, thereby significantly improving mixing efficiency. In contrast, the left–right filling method exhibits clear shortcomings during the initial mixing stage. At 2 s, materials are mainly piled on the left and right sides of the mixer, while the front–back and vertical motions of the blades are less effective in generating lateral shearing. As a result, effective convective circulation is difficult to establish early on, extending the time required for thorough mixing. Even at 60 s, the mixing effect under this method remains inferior to the other two approaches. This difference arises primarily because the left–right filling method fails to capitalize on the directional dynamics of the blades, requiring more time for the materials to be engaged in the active mixing zone during the initial phase.

Figure 10 illustrates the particle motion trajectories during the mixing process under the top–bottom filling method, with time intervals ranging from 3 s to 60 s. By analyzing this figure, the evolution of particle motion and changes in mixing state throughout the process can be clearly observed. The following discussion analyzes the mixing behavior at different time intervals, exploring how particle dynamics affect mixing uniformity. In the early stage of mixing (3–5 s), due to the material distribution characteristics of the top–bottom filling method, fine aggregates are primarily located in the upper part of the mixing container, while coarse aggregates are concentrated in the lower part. The motion of the mixing blades begins to drive the upper-layer material downward, allowing it to infiltrate the lower layer, while simultaneously pushing the coarse aggregates upward. However, the overall flow remains slow at this stage. Interactions between particles are still limited, and the material distribution largely reflects the initial layered state, with no significant mixing achieved. From the figure, it can be seen that particles start forming preliminary convection along the rotation direction of the blades, but the mixing uniformity remains low, and particle stratification is still evident.

When mixing time increases to 10 and 20 s, material fluidity improves, and particles begin to exhibit more vigorous circulatory motion under the influence of the mixing blades. At this stage, the shearing and pushing effects of the blades on the upper and lower material layers become more pronounced. Fine aggregates gradually infiltrate the coarse aggregate layer, while coarse aggregates are lifted into the upper region by the blade motion. The particle motion trajectories shown in the figure reveal a clearer convective circulation pattern. The interactions among materials intensify, the frequency of particle collisions increases, and the overall mixing effect improves progressively. Although mixing uniformity is significantly enhanced during this phase, a fully homogeneous distribution has not yet been achieved. Between 30 and 40 s, the material flow state becomes more stable, and particle trajectories appear more defined. The blades generate a strong convective structure, ensuring the even distribution of fine and coarse aggregates throughout the container. As mixing time progresses, inter-particle mixing further intensifies, and particle positions become increasingly randomized. The initial stratification essentially disappears. At this point, the circulatory motion within the mixer leads to a relatively uniform distribution of particles of varying sizes, and mixing uniformity increases substantially, reaching an ideal state. The figure shows the formation of complete convection loops within the mixer, and the random motion of particles effectively enhances the mixing process. In the final stage of mixing (50–60 s), the mixing effect stabilizes, and the particle distribution reaches a high degree of uniformity. The shearing action of the blades and the frequent particle collisions have been fully realized. The material is now uniformly distributed throughout the entire mixing space. While particle circulation continues, the overall degree of mixing

no longer changes significantly, indicating that the desired mixing uniformity has been achieved. At this stage, the primary role of continued mixing is to maintain uniformity rather than further improve it.

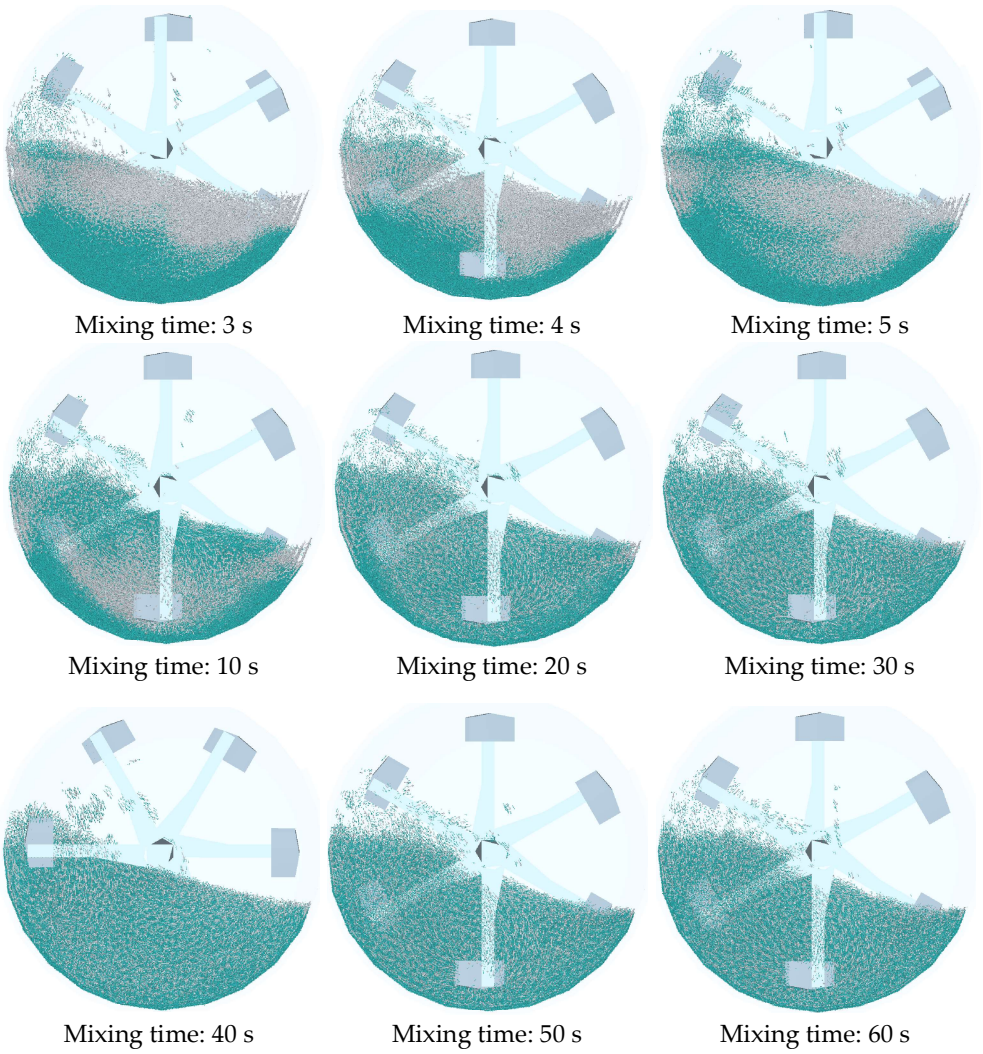

Figure 10. Vector diagram of particle motion during material mixing under upper and lower filling modes (side view).

Analysis of Figure 10 indicates that under the top–bottom filling method, the shearing and pushing actions of the mixing blades effectively promote the mixing of materials from the upper and lower layers. As the mixing time increases, a stable convective circulation gradually forms within the mixer, transitioning the material distribution from stratified to uniform. By the time mixing reaches 60 s, the mixing uniformity has achieved a high level, demonstrating that the top–bottom filling method significantly enhances mixing efficiency. This process clearly illustrates the relationship between particle motion trajectories and the evolution of mixing uniformity, providing valuable guidance for the optimization of mixing process design.

Figure 11 presents the particle motion trajectories and mixing states during the mixing process under the front–back filling method. The sequence covers mixing times from 3 s to 60 s, capturing the dynamic evolution of particle behavior. By examining particle distribution and motion at different time points, a detailed analysis of the mixing process under the front–back filling method can be conducted, alongside an exploration of the relationship between particle trajectories and changes in mixing uniformity. In the early

mixing stage (3–5 s), materials are mainly concentrated in the front and rear regions of the mixing container, with coarse and fine aggregates relatively segregated across these regions. As the mixing blades begin to rotate, they start to drive the material from the front and rear toward the center, initiating preliminary convective circulation. At this point, due to the initially separated distribution, mixing effectiveness is limited, and no significant uniform distribution is observed. The figure shows particle accumulation in the front and rear zones, with evident layering and low mixing uniformity. When the mixing time increases to 10 and 20 s, the particle motion changes markedly. The rotation of the blades drives the material into more pronounced circulatory flow, drawing particles from the front and rear toward the center, where they begin to interpenetrate and mix. The figures reveal enhanced material fluidity inside the mixer and the emergence of initial convective patterns. Fine aggregates begin to sink and diffuse, while coarse aggregates are lifted and mixed in, leading to a more balanced particle distribution. At this stage, mixing uniformity is significantly improved, although it still falls short of the ideal state.

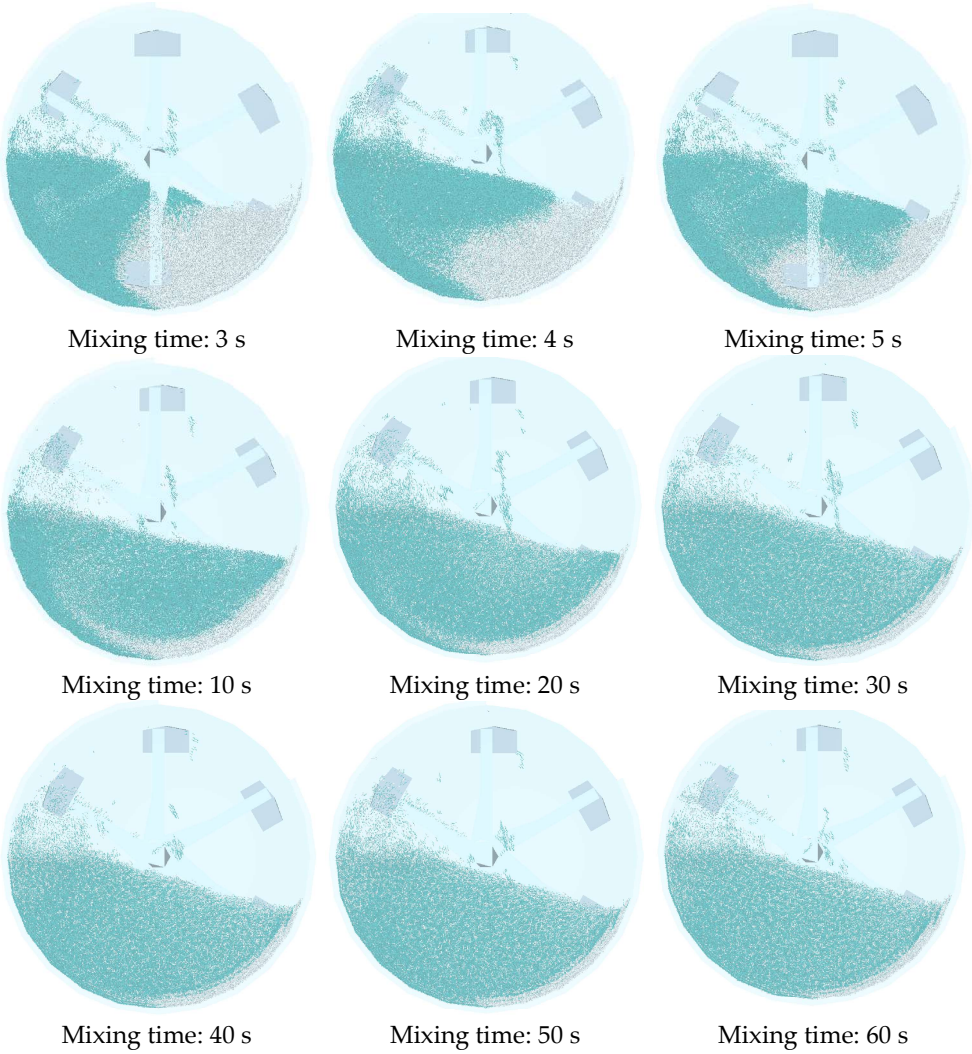

Figure 11. Vector diagram of particle motion during material mixing under pre- and post-filling modes (side view).

As mixing time further increases to the 30–40 s range, a stable convective circulation structure forms within the mixer. As shown in Figure 10, particle motion trajectories become more distinct, and the circulation range within the mixer expands. Particles from the front and rear regions gradually blend, marking the transition from a layered to a

uniformly distributed state. The continued rotation of the mixing blades intensifies relative motion and collisions among particles, promoting uniform distribution of coarse and fine aggregates. During this stage, mixing uniformity improves significantly, the layering phenomenon is nearly eliminated, and the mixing performance becomes optimal. In the later stage of mixing (50–60 s), the mixed state of the material stabilizes, and particles are uniformly distributed throughout the mixer. Figure 11 shows that the flow paths of the material form a closed convective loop, and while the frequency of relative motion among particles decreases, the overall mixing state remains unchanged. At this point, the role of the mixing blades shifts from enhancing mixing to maintaining uniformity. The mixing uniformity reaches its highest level, demonstrating that the front–back filling method effectively promotes mixing uniformity and achieves sufficient mixing in a relatively short time.

Figure 12 presents the particle motion vector diagrams under the left–right filling method across different mixing durations. By observing particle distribution and motion from 3 to 60 s, the evolution of particle trajectories and mixing uniformity throughout the process can be analyzed. The following section focuses on particle behavior at different time intervals to examine how the left–right filling method affects mixing performance. In the early mixing stage (3–5 s), materials are mainly concentrated on the left and right sides of the mixer. The blades begin pushing material from both sides toward the center. However, due to the initial lateral separation, particle motion is constrained, and mixing between materials is limited, with particles remaining relatively independent. During this phase, mixing uniformity is low, and the stratification between the left and right sides is obvious. The shearing and pushing effects of the blades have not yet fully developed, and particle movement remains largely unidirectional without significant convective circulation. As a result, mixing is suboptimal, and the material distribution is still dominated by the initial filling layout. When mixing time reaches 10–20 s, blade rotation accelerates, gradually driving materials from both sides toward the center. Preliminary convective structures begin to form, with increasing material interpenetration. Coarse and fine aggregates begin to mix. Although ideal mixing has not yet been achieved, particle interactions become more frequent, and mixing uniformity shows improvement. At 20 s, more defined arched flow trajectories can be observed: particles rise from both sides and descend toward the center, forming the early stages of a convective loop. Nevertheless, the particle distribution remains uneven, and fusion between materials from both sides is still limited, resulting in a slow increase in uniformity.

During the mid-stage of mixing (30–40 s), particle motion becomes more active. Blades induce more pronounced circular flows, with particles circulating both upward and downward within the mixer. The distribution of materials becomes increasingly uniform, and interactions between coarse and fine aggregates increase significantly. Stratification is nearly eliminated, and mixing uniformity improves markedly. These results show that although the left–right filling method is less favorable for mixing initially, prolonged blade movement gradually promotes uniform distribution and enhances mixing performance. However, compared to the other filling methods, the mixing rate under the left–right approach remains slower—likely due to the mismatch between initial material placement and blade motion direction. In the final mixing stage (50–60 s), the material reaches its best mixing state. Particles are evenly distributed throughout the container, and a stable convective circulation is established. At this point, inter-particle interactions between coarse and fine aggregates are maximized. Collisions and friction among particles randomize their distribution, achieving near-complete mixing. Figure 11 shows that with extended mixing time, the left–right filling method can also reach an ideal mixing effect, albeit requiring a

longer duration. During this stage, mixing mainly serves to maintain the already uniform distribution. Particle motion trajectories stabilize, and the mixing efficiency levels off.

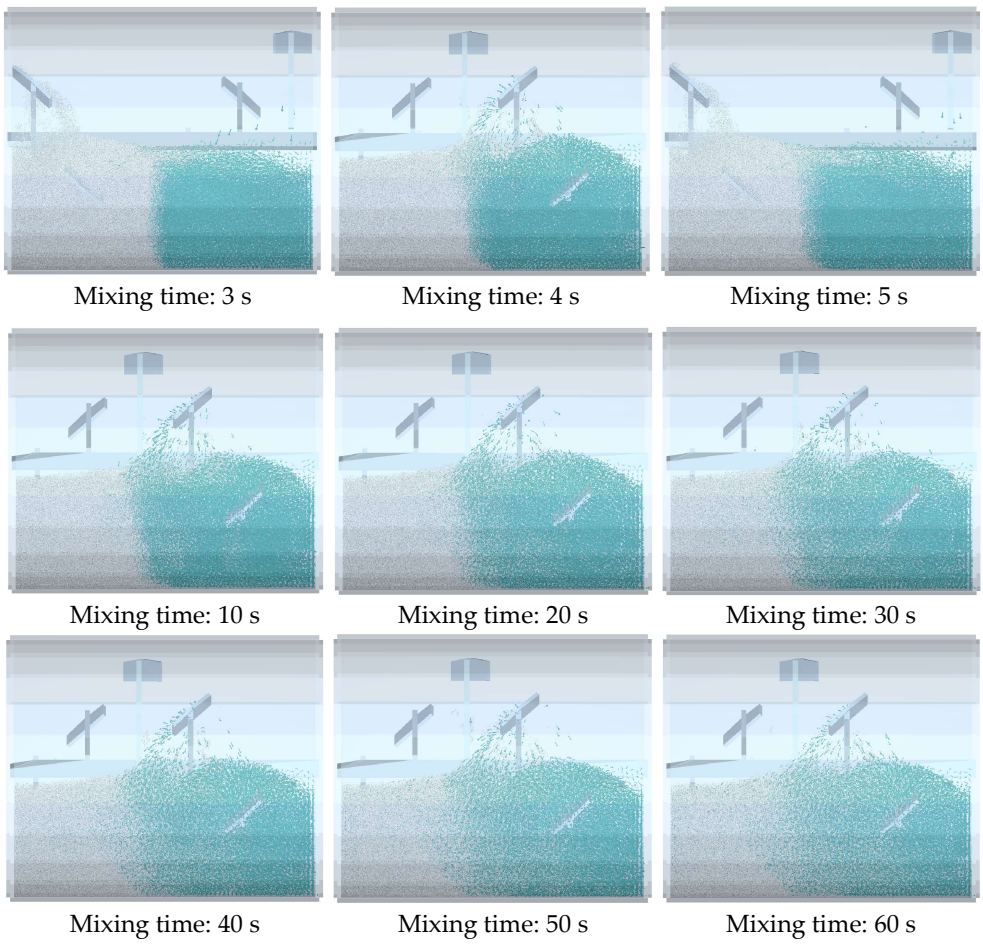

Figure 12. Vector diagram of particle motion during material mixing under left and right filling modes (front view).

By comparing Figures 10–12, the following conclusions can be drawn: Under the top–bottom filling method (Figure 10), the material is distributed with fine aggregates in the upper layer and coarse aggregates in the lower layer. This arrangement is well aligned with the movement direction of the mixing blades. Once mixing begins, the blades quickly drive the upper materials downward and the lower materials upward, forming a strong vertical convective circulation. Particle interpenetration and uniform distribution are rapidly achieved, resulting in a significant increase in mixing uniformity within a short time. By the mid-to-late mixing stage (around 30 s), the materials have basically reached an ideal homogeneous state. The top–bottom filling method performs best in terms of mixing efficiency and uniformity and is suitable for scenarios with high requirements for mixing homogeneity. In the front–back filling method (Figure 12), materials are distributed across the front and rear regions of the mixer. The mixing blades begin pushing the materials from both sides toward the center, gradually forming a convective circulation. Although the initial distribution is not as perfectly aligned with blade motion as the top–bottom method, the mixing effect improves over time. Especially after 20 s, particles begin to form relatively stable circulation within the container. By the later mixing stages, the coarse and fine aggregates are evenly distributed, and the stratification disappears. Overall, the front–back filling method results in good mixing uniformity and requires a moderate mixing time, although the mixing speed in the early stage is slightly slower. In the left–right

filling method (Figure 12), materials are initially placed on the left and right sides of the mixer. This arrangement does not match the movement direction of the mixing blades, leading to pronounced initial stratification and poor mixing performance. As mixing begins, materials on both sides are slowly driven by the blades, and it takes a long time for effective convective circulation to form. A relatively long mixing time (usually more than 30 s) is needed to achieve a satisfactory mixing state. Therefore, compared to the top–bottom and front–back methods, the left–right filling method shows certain disadvantages in terms of mixing efficiency and uniformity. It is more suitable for scenarios where lower mixing uniformity is acceptable and longer mixing durations are permissible.

In summary, each of the three filling methods has its own strengths and weaknesses. The top–bottom filling method performs best in terms of both mixing uniformity and efficiency; the front–back filling method is slightly inferior but still achieves good mixing performance; the left–right filling method performs poorly in terms of mixing speed and uniformity. The appropriate filling method can be reasonably selected based on specific mixing needs and efficiency requirements to optimize the mixing effect.

Figure 13 shows the power consumption under different filling methods. It can be observed that the power consumption for all three filling methods increases rapidly during the initial mixing stage (0–5 s). This phase corresponds to the startup period of the mixer, where the blades need to overcome the static resistance of the material and initiate flow, resulting in a sharp rise in power consumption. Specifically, under the front–back filling method, power consumption increases the fastest between 0 and 2 s, reaching approximately 1200 W. In contrast, the top–bottom and left–right filling methods show slightly slower increases in power consumption, which may be related to the initial distribution states of the material under different filling methods. In the front–back filling method, the material is concentrated in the front and rear regions of the mixer, allowing the blades to directly exert shearing forces on the material at startup, leading to higher initial power consumption.

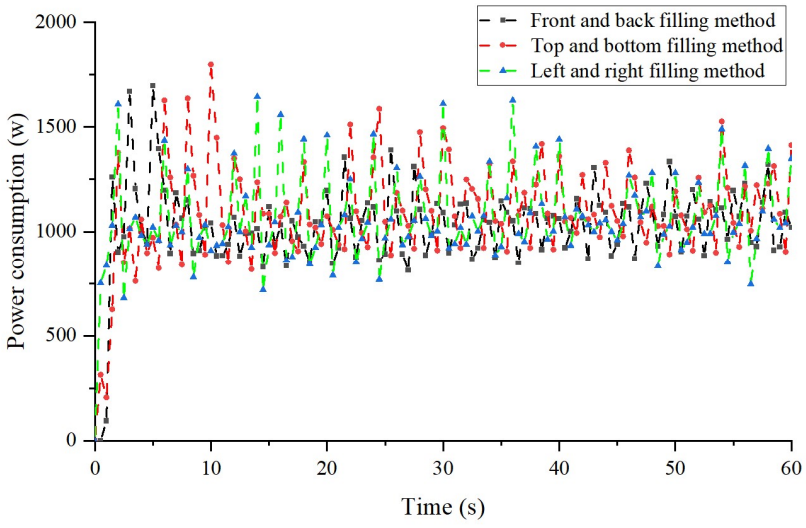

Figure 13. Power consumption under different filling methods.

As the mixing time increases (5–30 s), power consumption under all three filling methods exhibits some fluctuations but generally tends to stabilize. These fluctuations are mainly caused by the collisions between coarse and fine aggregates and the changes in their accumulation states during the mixing process. Compared to the top–bottom and left–right filling methods, the front–back filling method shows smaller power fluctuation amplitudes, indicating that the material flow is more stable and the resistance to the blades changes

less under this filling pattern. The top–bottom and left–right filling methods show larger fluctuations, with pronounced peaks particularly at 10, 20, and 30 s. This phenomenon may be related to the formation of localized accumulations during mixing. In the case of the top–bottom filling method, especially, vertical accumulation and shearing cause significant variations in blade loading, resulting in frequent power fluctuations.

In the later stage of mixing (30–60 s), power consumption under all three filling methods generally stabilizes around 1000 W. At this point, the materials in the mixer are fully engaged in the mixing cycle, and interactions among particles as well as the shearing effect of the mixing blades have become stable, leading to reduced fluctuations in power consumption. However, the left–right filling method still exhibits greater fluctuations in this phase compared to the front–back and top–bottom methods, indicating relatively poorer stability in the mixing process. These larger fluctuations may result from the initial left–right distribution of the material, which requires the blades to exert more time and energy to drive the material on both sides into uniform mixing, thereby causing greater variations in power consumption.

4.2.2. Effect of Different Rotational Speeds on Work Performance

Figure 14 shows the material distribution after 60 s of mixing at different rotation speeds. From the figure, it can be seen that as the mixing speed increases, the mixing effect of the material improves significantly. At a rotation speed of 20 rpm, the material exhibits obvious stratification, with fine and coarse aggregates distributed unevenly within the mixer. Under low-speed conditions, the shearing and pushing effect of the blades on the material is relatively weak, preventing the formation of sufficient convective circulation. As a result, the mixing between coarse and fine particles is poor. Mixing at 20 rpm is mainly characterized by local blending, with limited overall material turnover and dispersion, leading to an unsatisfactory mixing result. When the speed increases to 30 rpm, the mixing performance improves markedly. The faster rotation of the blades enhances their shearing effect on the material and improves material flowability within the mixer. Interactions between coarse and fine aggregates become more frequent, and the mixing uniformity is significantly better than that at 20 rpm. At 30 rpm, the mixer can effectively induce both vertical and horizontal material flow, resulting in a more uniform distribution throughout the container. The overall mixing effect is notably improved, especially during the mid-to-late mixing stages, when particle collisions and relative movement become more frequent and the mixture approaches an ideal state. When the rotation speed is further increased to 40 rpm, the material achieves its best mixing condition. The higher mixing speed allows the blades to exert a stronger shearing and pushing force, greatly increasing the rate of material turnover and dispersion within the mixer. At 40 rpm, the rapid blending of coarse and fine aggregates, along with enhanced spatial randomization of particles, enables the mixture to reach uniformity in a shorter period. However, it is important to note that although a speed of 40 rpm improves mixing efficiency, excessively high rotation speeds may introduce other issues, such as increased energy consumption, accelerated wear of the mixing blades, and potential overmixing of the material. Therefore, in practical engineering applications, an appropriate mixing speed should be selected based on a balanced consideration of mixing efficiency and energy consumption.

Figure 15 illustrates the power consumption at different rotation speeds. It can be observed that under all three speed conditions, power consumption increases rapidly during the initial mixing stage (0–5 s). This phase corresponds to the startup period of the mixer, during which the mixing blades must overcome the static resistance of the material and initiate movement, resulting in a sharp rise in power consumption. At a rotation speed of 20 rpm, the power consumption increases more gradually during the initial stage,

with a peak value of approximately 500 W. In contrast, the initial power consumption is significantly higher at 30 rpm and 40 rpm, particularly under the high-speed condition of 40 rpm, where the peak power exceeds 1500 W. This phenomenon indicates that at higher rotation speeds, the mixing blades exert stronger shearing and pushing forces on the material, thus requiring more energy to overcome the initial material resistance.

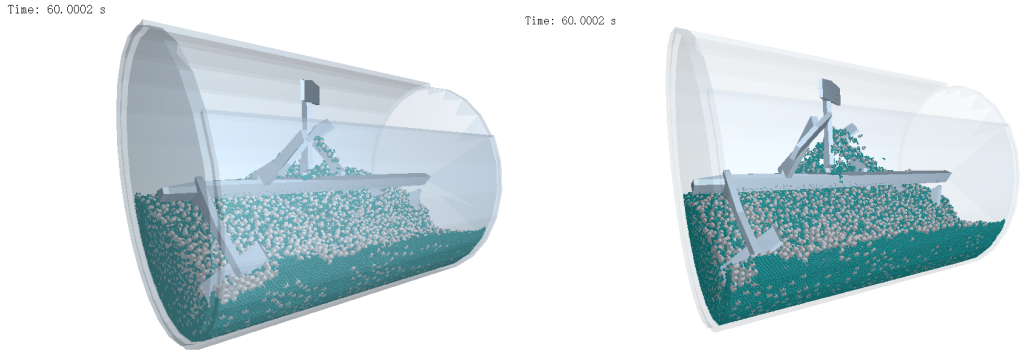

(**a**) The rotational speed is 20 rpm (**b**) The rotational speed is 30 rpm

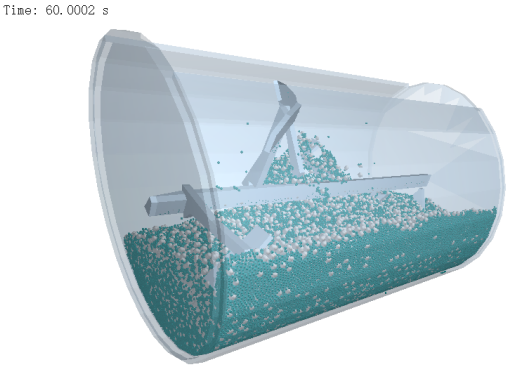

(**c**) The rotational speed is 40 rpm

Figure 14. Final mixing effect under different rotation speeds.

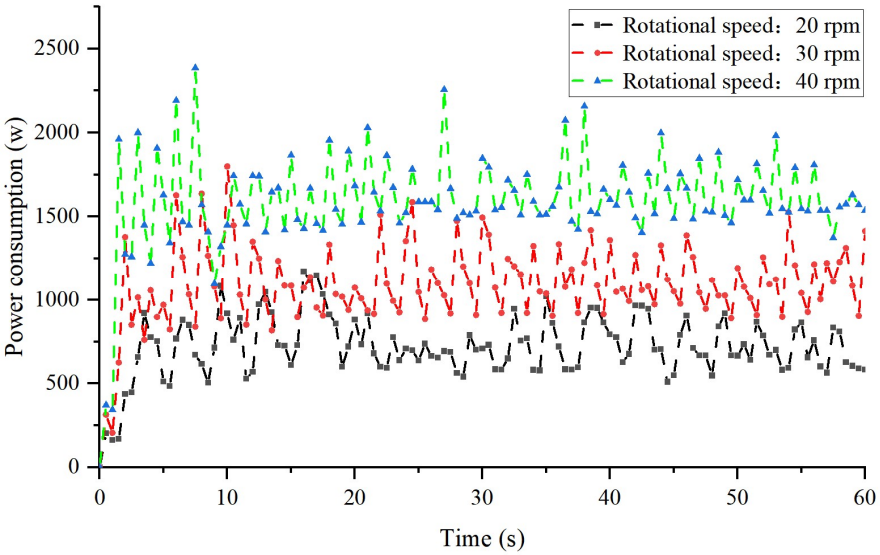

Figure 15. Power consumption under different rotation speeds.

During the mid-stage of mixing (5–30 s), power consumption gradually tends to stabilize but still exhibits some fluctuations. As the rotation speed increases, the amplitude of these fluctuations also grows. Under the 20 rpm condition, power consumption fluctuates only slightly, averaging between 500 W and 1000 W. This indicates that at low speeds, the

mixer's interaction with the material is relatively gentle, the material flow is more stable, and the load on the mixing blades changes only minimally. In contrast, at higher speeds of 30 rpm and 40 rpm, power consumption fluctuations are more pronounced—especially at 40 rpm, where the fluctuation range falls between 1000 W and 2000 W. These larger variations reflect the more intense shearing and collision between the blades and the material at high rotation speeds, resulting in more frequent changes in energy demand.

In the later stage of mixing (30–60 s), power consumption under all three speed conditions remains relatively stable, though notable differences persist. At 20 rpm, power consumption remains the lowest, averaging around 700 W, whereas at 30 rpm and 40 rpm, the average power consumption is approximately 1200 W and 1600 W, respectively. This suggests that at the same mixing duration, higher rotation speeds require more energy to maintain material mixing and flow. The increased energy consumption primarily results from the continuous shearing and high-frequency collisions between the blades and the material at higher speeds. Therefore, although higher speeds may enhance mixing efficiency, they are also accompanied by significantly higher energy demands.

4.2.3. Effect of Different Coarse Aggregate Particle Sizes on Workability

Figure 16 shows the mixing performance of materials under three different coarse aggregate particle sizes: 9 mm, 12 mm, and 15 mm. A comparative analysis reveals that as the coarse aggregate size increases, the overall mixing performance deteriorates, specifically manifested by increased non-uniformity in the spatial distribution of coarse and fine aggregates within the mixer. The following provides a detailed analysis of this phenomenon and explains the negative impact of increasing aggregate size on mixing performance. When the coarse aggregate size is 9 mm, the mixing effect is relatively good. At this size, the smaller particles allow for more frequent relative motion among them. The mixing blades are able to shear and push a greater number of particles into overturning and circulation. Under these conditions, strong convective loops are formed within the mixer, and coarse and fine aggregates penetrate each other spatially, ultimately achieving a relatively uniform mixing state. The smaller particle size also enables the aggregates to be more effectively mobilized by the mixing blades, thereby accelerating the mixing rate and allowing a near-ideal mixed state to be reached within 60 s. When the particle size increases to 12 mm, the mixing performance declines. Larger coarse aggregates exhibit greater inertia and mass during mixing, which slows their response to the shearing action of the blades and makes it harder for them to be quickly drawn into convective motion. Although 12 mm aggregates can still be partially overturned and mixed by the blades, their mixing uniformity is clearly inferior to that observed with 9 mm particles. This difference primarily arises from the increased mass of the larger aggregates, making them more difficult to mobilize and thus negatively impacting the overall mixing process. When the particle size further increases to 15 mm, the mixing effect worsens significantly. At this point, the large particle size causes more pronounced stratification at the early stage of mixing. Due to their greater volume and mass, the blades are less able to effectively shear and propel these particles. The interpenetration between coarse and fine aggregates decreases further, and mixing uniformity drops considerably. The large size of the coarse aggregates not only makes it more difficult for them to be incorporated into the convective flow but also increases the likelihood of localized accumulation, which can further hinder the mixing process. Because of their high inertia, large particles exhibit poor mobility within the mixer and are difficult to uniformly mix with finer materials in a short period. This is the main reason why the 15 mm particle size results in the poorest mixing performance.

Figure 17 shows the power consumption under different coarse aggregate particle sizes. It can be observed that during the initial mixing stage (0–5 s), the power consumption

for all three aggregate sizes rises sharply. This stage corresponds to the startup phase of the mixer, during which the mixing blades must overcome the static resistance of the material to initiate flow. The larger the particle size of the coarse aggregate, the greater the mass and inertia of the particles, requiring the blades to apply higher shearing forces to overcome the initial resistance. As a result, this leads to higher power consumption. For the 9 mm particle size, the initial power consumption ranges between 500 W and 1000 W. In contrast, for the 12 mm and 15 mm particle sizes, the peak initial power consumption exceeds 1500 W and 2000 W, respectively. This indicates that larger-sized coarse aggregates generate greater resistance during the startup phase of mixing, thereby demanding more energy input.

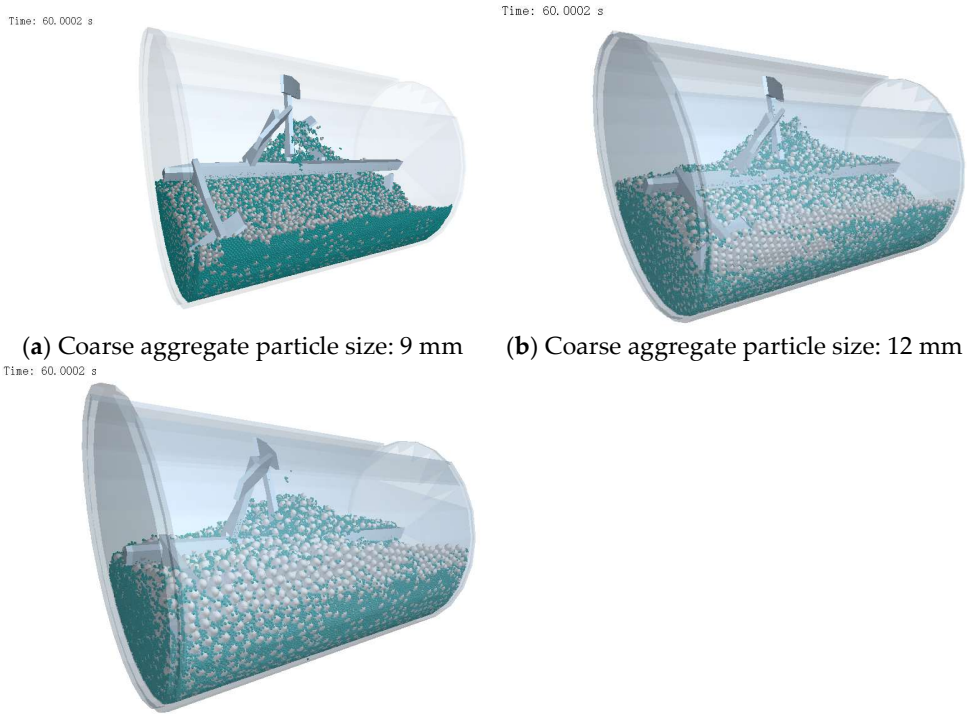

(**a**) Coarse aggregate particle size: 9 mm (**b**) Coarse aggregate particle size: 12 mm

(**c**) Coarse aggregate particle size: 15 mm

Figure 16. Final mixing effect under different coarse aggregate particle sizes.

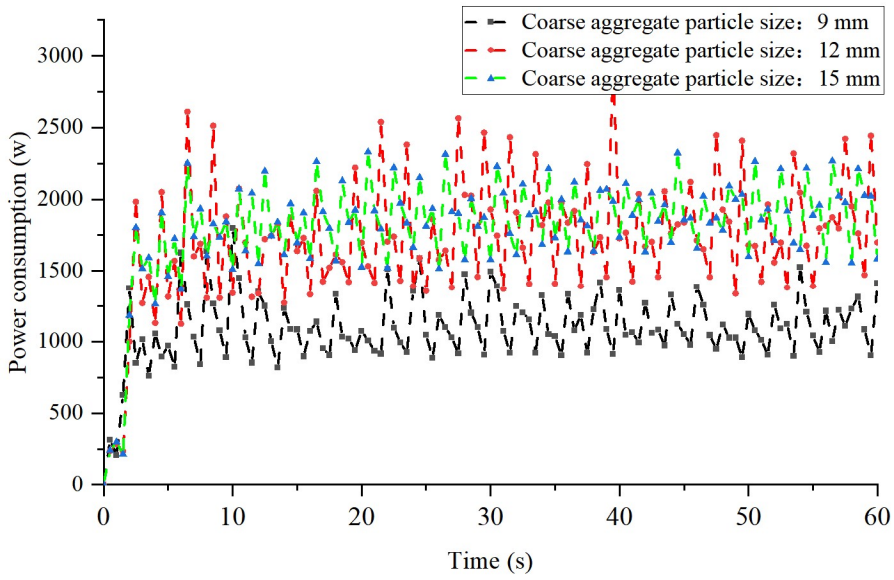

Figure 17. Power consumption under different coarse aggregate particle sizes.

During the mid-stage of mixing (5–30 s), the power consumption for different particle sizes gradually stabilizes, but significant differences remain. For the 9 mm particle size, power consumption exhibits relatively small fluctuations, with an average around 1000 W. This indicates that smaller coarse aggregates have better flowability during mixing, allowing the blades' shearing and pushing actions to more effectively mobilize the material. In contrast, for the 12 mm and 15 mm particle sizes, power consumption shows larger fluctuations, with average values maintained above 1500 W and 2000 W, respectively. These larger fluctuations reflect more intense collisions between the larger aggregates and the blades, as well as more pronounced friction and accumulation among the particles. Due to their greater mass and inertia, larger aggregates require more energy for the blades to drive them into motion, resulting in significantly higher power consumption.

In the later stage of mixing (30–60 s), power consumption across all three particle sizes remains relatively stable, but the differences are still evident. The 9 mm aggregates maintain lower and more stable power consumption, while the 12 mm and 15 mm aggregates continue to show higher consumption and more frequent fluctuations. Particularly in the case of the 15 mm aggregates, peak power consumption even exceeds 2500 W, indicating poor flowability within the mixer. Local accumulation and particle collisions exert considerable load on the blades. The difficulty in mobilizing large aggregates effectively contributes to increased power consumption. This phenomenon further confirms the negative impact of increasing coarse aggregate size on mixing efficiency, as it not only increases energy demand but may also compromise the uniformity and stability of the mixing process.

Figure 18 quantitatively compares the average power consumption of three factors (filling method, rotational speed, and aggregate size), revealing the energy-dominant mechanism. Among filling methods, top–bottom filling showed the highest average power consumption (~1200 W) due to strong shear effects (requiring overcoming gravitational potential barriers) but achieved an optimal mixing degree (0.9). In contrast, left–right filling had the lowest power consumption (~900 W) but poorest mixing performance (0.4). Regarding rotational speed, 40 rpm's average power consumption (1600 W) was 33% higher than 30 rpm (1200 W), while providing only 5% mixing improvement, confirming 30 rpm as the energy efficiency inflection point. Aggregate size exhibited the most significant impact: 15 mm aggregates showed 100% higher average power consumption (~2000 W) than 9 mm aggregates (~1000 W) due to enhanced collision dissipation of high-inertia particles, while mixing degree decreased to 0.6.

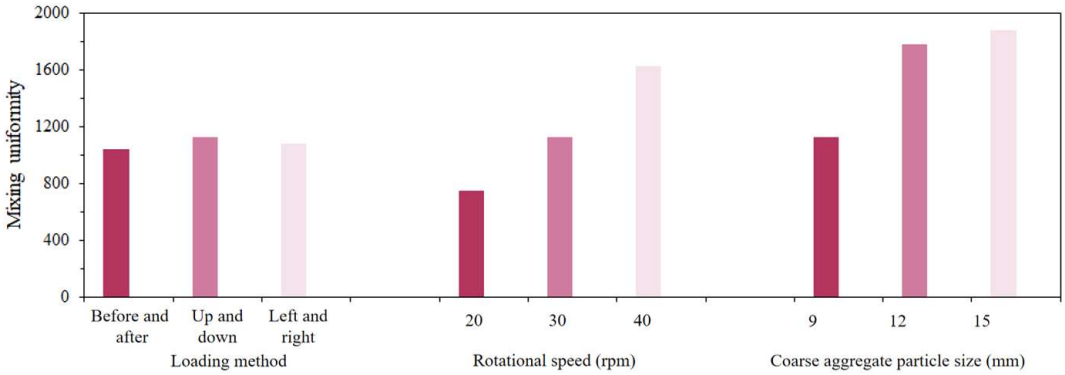

Figure 18. Average power consumption under different factors.

5. Conclusions

This study conducted a systematic simulation analysis of the working performance of a single horizontal shaft forced mixer based on the Discrete Element Method (DEM),

with a particular focus on the effects of filling method, mixing speed, and coarse aggregate particle size on mixing uniformity. The main conclusions are as follows:

(1) Significant impact of filling method on mixing efficiency: The top–bottom filling method promotes rapid mixing of fine and coarse aggregates by establishing vertical convective circulation, achieving a mixing uniformity above 0.9. The front–back filling method ranks second, while the left–right method performs the worst, with a mixing uniformity of only 0.4 due to the misalignment between initial material distribution and blade motion direction. In practical applications, top–bottom or front–back filling should be prioritized to improve efficiency.

(2) Optimal mixing speed range: A moderate speed of 30 rpm offers the best balance between mixing efficiency and energy consumption, achieving a mixing uniformity close to 0.9. At 20 rpm, insufficient shear force leads to poor mixing, while 40 rpm, though more efficient, significantly increases energy consumption and may cause secondary segregation of particles.

(3) Sensitivity to coarse aggregate size: Smaller coarse aggregate sizes (9 mm) improve particle mobility, resulting in a mixing uniformity of 0.9. When the particle size increases to 15 mm, enhanced inertia and localized accumulation reduce the uniformity to 0.6. It is recommended that coarse aggregate size be controlled in practical applications to optimize mixing performance.

This study reveals the mechanisms by which key parameters influence the mixing performance of single-shaft mixers, providing theoretical support for equipment design and process optimization. However, the research has certain limitations, such as not accounting for complex conditions like material moisture and viscosity. Future studies may incorporate multi-physics coupling methods (e.g., CFD-DEM) to further investigate mixing mechanisms involving non-spherical particles and multiphase flows, thereby expanding the model's applicability and enhancing its engineering relevance.

Author Contributions: Methodology, G.M.; Software, H.Y.; Formal analysis, H.Y.; Investigation, G.M.; Data curation, G.M.; Writing – original draft, W.Z.; Writing – review & editing, H.Y.; Supervision, W.Z.; Funding acquisition, G.M. All authors have read and agreed to the published version of the manuscript.

Funding: This study was funded by projects such as the National Natural Science Foundation of China (Grant No. 52304237).

Data Availability Statement: The original contributions presented in the study are included in the article, further inquiries can be directed to the corresponding author.

Conflicts of Interest: Authors Haipeng Yang and Wei Zhao were employed by the company Zaozhuang Mining Group Xin'an Coal Industry Co., Ltd. The remaining author declares that the research was conducted in the absence of any commercial or financial relationships that could be construed as a potential conflict of interest.

References

1. Zhang, Z.; Yang, L. Numerical simulation analysis of mixing performance of forced single horizontal shaft mixer. *J. China Univ. Min. Technol.* **2020**, *47*, 77–82.
2. Li, H.; Wang, L. Research on Energy Conservation and Emission Reduction of Single Axis Concrete Mixer. *J. Build. Sci. Eng.* **2017**, *39*, 30–35.
3. Zheng, X.; Huang, S. Development of concrete mixing equipment and improvement of single horizontal shaft mixer. *J. Civ. Eng.* **2016**, *28*, 41–45.
4. Chen, T.; Wang, X.; Li, Q. Energy-saving and High-performance Improvements of Single Horizontal Shaft Concrete Mixers. *Mater. Sci. Eng.* **2019**, *7*, 215–223.

5. Smith, J.; Brown, R. Structural Design and Optimization of Single-Shaft Concrete Mixers. *J. Constr. Eng. Manag.* **2017**, *143*, 102–107.
6. Zhao, L. Research on Mixing Inefficient Zones and Their Elimination Methods. Master's Thesis, Chang'an University, Xi'an, China, 2005.
7. Zhao, W. Research on Optimization of Mixing Device Parameters. Master's Thesis, Chang'an University, Xi'an, China, 2005.
8. Feng, Z.; Chen, J. The mixing process and simulation of concrete. *J. Xi'an Jiaotong Univ.* **1997**, *17*, 71–76.
9. Feng, Z. *Concrete Mixing Theory and Equipment*; People's Communications Press: Beijing, China, 2001.
10. Liu, H.; Ma, D. Influence of Using Parameters on Stirring Uniformity of Mixer. *J. Wuhan Univ. Technol. Mater. Sci.* **2011**, *26*, 172–175. [CrossRef]
11. Wang, D.; Yu, K. Working principle and parameter optimization of single axis horizontal fully mixed feed mixer. *J. Northeast. Agric. Univ.* **2008**, *5*, 128–130.
12. Laurent, B.; Bridgwater, J.; Parker, D. Motion in a particle bed agitated by a single blade. *AIChE J.* **2000**, *46*, 1723–1734. [CrossRef]
13. Li, Q. Theoretical Study on Particle Collapse Flow Behavior in Fluid Based on CFD-DEM Method. Master's Thesis, Lanzhou University, Lanzhou, China, 2021.
14. Cundall, P.A. A computer model for simulating progressive, large-scale movement in blocky rock system. *Proc. Int. Symp. Rock Mech.* **1971**, *8*, 129–136.
15. Cundall, P.A.; Strack, O.D. A discrete numerical model for granular assemblies. *Geotechnique* **1979**, *29*, 47–65. [CrossRef]
16. Cai, R.; Zhao, Y. An experimentally validated coarse-grain DEM study of monodisperse granular mixing. *Powder Technol.* **2020**, *361*, 99–111. [CrossRef]
17. Lischka, C.; Nirschl, H. Simulation of an intensive lab mixer for dry mixing of Li-ion cathode materials via the discrete element method. *Particuology* **2025**, *104*, 52–67. [CrossRef]
18. Zou, J.; Li, W.; Song, Y.; Sun, J. Parameter optimization of plow mixer structure based on EDEM. *KSCE J. Civ. Eng.* **2024**, *28*, 3782–3790. [CrossRef]
19. Boonkanokwong, V.; Khinast, J.G.; Glasser, B.J. Scale-up and flow behavior of cohesive granular material in a four-bladed mixer: Effect of system and particle size. *Adv. Powder Technol.* **2021**, *32*, 4481–4495. [CrossRef]
20. Karkala, S.; Ramachandran, R. Investigating the effects of material properties on the mixing dynamics of cohesive particles in a twin screw mixer using a discrete element method approach. *Powder Technol.* **2022**, *409*, 117762. [CrossRef]
21. Long, J.; Wang, C.; Zhu, J.; Zhan, X.; Sun, Z.; Shen, B.; Li, X. Discrete element simulation for mixing performances and power consumption in a twin-blade planetary mixer with non-cohesive particles. *Adv. Powder Technol.* **2022**, *33*, 103437. [CrossRef]
22. Bao, M.; Lin, J.; Zhang, F.; Yang, J. Discrete element method study of parameter optimization and particle mixing behaviour in a soil mixer. *Particuology* **2023**, *81*, 1–14. [CrossRef]
23. Wang, D.; Yu, J.; Lv, Z.; Song, Y.; Huang, H.; Tian, H.; Wang, H.; Su, B. Effect of impeller rotational speed and paddle angle on binary mixing in a paddle mixer based on DEM. *Particuology* **2025**, *102*, 178–189. [CrossRef]
24. Tan, Y.; Dahlenburg, M.; Fottner, J.; Kessler, S. Influencing factors of the mixing performance of a near-nozzle continuous mixer for 3D concrete printing: An analysis based on spatial Lacey mixing index (SLMI). *Powder Technol.* **2022**, *403*, 117414. [CrossRef]
25. Crowe, C.T.; Sommerfeld, M.; Tsuji, Y. *Multiphase Flows with Droplets and Particles*; CRC Press: Boca Raton, FL, USA, 1997.
26. Wang, S.; Li, H.; Tian, R. Numerical simulation of particle flow behavior in a screw conveyor using the discrete element method. *Particuology* **2019**, *43*, 137–148. [CrossRef]
27. EDEM. EDEM 2022.2 Theory Reference Guide; 2022. Available online: https://2022.help.altair.com/2022.2/EDEM/Simulator/#t=Introducing_EDEM.htm (accessed on 22 July 2025).